Check for updates

Ag$_8$SnS$_6$: a new IR solar absorber material with a near optimal bandgap†

Patsorn Boon-on,[a] Belete Asefa Aragaw,[ab] Chun-Yen Lee,[a] Jen-Bin Shi[c] and Ming-Way Lee [ID] *[a]

We report the synthesis and photovoltaic properties of a new ternary solar absorber – Ag$_8$SnS$_6$ nanocrystals prepared by successive ionic layer adsorption reaction (SILAR) technique. The synthesized Ag$_8$SnS$_6$ nanocrystals have a bandgap E_g of 1.24–1.41 eV as revealed from UV-Vis and external quantum efficiency (EQE) measurements. Its photovoltaic properties were characterized by assembling a liquid-junction Ag$_8$SnS$_6$ sensitized solar cell for the first time. The best cell yielded a J_{sc} of 9.29 mA cm^{-2}, a V_{oc} of 0.23 V, an FF of 31.3% and a power conversion efficiency (PCE) of 0.64% under 100% incident light illumination using polysulfide electrolyte and Au counter electrode. The efficiency improved to 1.43% at a reduced light intensity of 10% sun. When the polysulfide was replaced by a cobalt electrolyte with a lower redox level, the V_{oc} increased to 0.54 V and PCE increased to 2.29% under 0.1 sun, a respectable efficiency for a new solar material. The EQE spectrum covers the spectral range of 300–1000 nm with a maximum EQE of 77% at λ = 600 nm. The near optimal E_g and the respectable photovoltaic performance suggest that Ag$_8$SnS$_6$ nanocrystals have potential to be an efficient IR solar absorber.

1. Introduction

Semiconductor nanocrystals are now receiving much research attention in the field of photovoltaics. This is due to the unique properties of semiconductor NC materials such as band gap tenability[1,2] and high absorption coefficient.[3] Moreover, multiple exciton generation effect and hot electron injection in these solar absorbers could improve the solar cell efficiency beyond the Shockley–Queisser limit.[4–9] Semiconductor nanocrystals materials can be prepared by solution-based processing, which has the advantages of ease of fabrication and low-cost over Si based solar cell processing.

A requirement for a good solar absorber material is that the energy gap E_g should be near 1.4 eV in order to produce a maximal output power.[10] To date, the most widely studied solar absorber materials have been the binary metal sulfides and selenides such as CdS, CdSe, PbS, PbSe, Sb$_2$S$_3$ and Ag$_2$S etc.[11–16] For a binary semiconductor, its E_g is a fixed value. Only a small number of binary semiconductor satisfies the E_g = 1.4 eV requirement. This limits the number of binary semiconductors suitable for solar absorbers. An advantage of ternary semiconductors is that E_g can be tuned by varying the ratios of the constituent elements, leading to formation of a broad range of new compounds that could be potential solar absorber materials. Solar cells based on ternary metal sulfides have been relatively less explored due to the difficulty in the material synthesis (the widely studied Cu–In–Se system being an exception).

The family of I–III/IV–VI (Cu- and Ag-based) ternary metal sulfides, such as AgInS$_2$,[17] AgBiS$_2$,[18] AgSbS$_2$,[19] Ag$_3$SbS$_3$,[20] CuInS$_2$,[16] Cu$_2$SnS$_3$ (ref. 21 and 22) and Cu$_4$SnS$_4$,[23,24] have been investigated for their applications in photovoltaics and photocatalytics. Among them, Ag$_8$SnS$_6$ owns several important properties such as an ideal E_g of 1.3–1.5 eV, which is near the optimal E_g of 1.4 eV for a solar cell, and high absorption coefficients of $\alpha \sim 10^4$ cm^{-1} in the visible range.[25] Moreover, the three elements contained in Ag$_8$SnS$_6$ – Ag, Sn and S – are nontoxic and environmentally friendly. Ag$_8$SnS$_6$ nanocrystals have been synthesized for various purposes[26–30] such as counter electrodes in dye-sensitized solar cells,[31] photocatalytic dye degradation,[32] photoelectrochemical salt-water splitting[33] and thermoelectrics.[34] Ag$_8$SnS$_6$ solar cells have recently been reported with an efficiency of 0.25%.[35] Here, we report the simple solution-based preparation of Ag$_8$SnS$_6$ nanocrystals and investigation of their photovoltaic properties. Ag$_8$SnS$_6$ nanocrystals were directly grown on the surfaces of mesoporous TiO$_2$ nanoparticles using the successive ionic layer adsorption and reaction (SILAR) technique. Liquid-junction quantum dot-sensitized solar cells based on Ag$_8$SnS$_6$ nanocrystals are demonstrated for the first time. The material crystal structure, morphology and optical property have been investigated. The dependence of

[a] Institute of Nanoscience, Department of Physics, National Chung Hsing University, Taichung 402, Taiwan. E-mail: mwl@phys.nchu.edu.tw

[b] Department of Chemistry, Bahir Dar University, P.O. Box 79, Bahir Dar, Ethiopia

[c] Department of Electronic Engineering, Feng Chia University, Taichung, 40724, Taiwan

photovoltaic performance on SILAR conditions, sun intensity and type of electrolyte have also been studied.

2. Experimental

2.1. Preparation of TiO$_2$ electrodes

Fluorine-doped tin oxide glass (FTO, Pilkington, sheet resistance ~ 7 Ω □$^{-1}$) was cleaned with acetone, methanol, and deionized water successively in an ultrasonic bath. It was then coated with three layers of TiO$_2$ film with different particle sizes and film thicknesses. First, a 90 nm thick compact TiO$_2$ film was made by spin-coating (2000 rpm, 1 min) a 0.2 M titanium tetraisopropoxide solution (TTIP) onto an FTO substrate, followed by annealing at 190 °C for 5 min. Next, a mesoporous TiO$_2$ (mp-TiO$_2$) layer (Dyesol 30NR-D, particle size 30 nm, ~10 μm thick) was coated on top of the compact layer by the doctor blade technique and heated at 125 °C for 5 min. Finally, a TiO$_2$ scattering layer (Dyesol WER2-O, particle size 300 nm, ~5 μm thick) was coated on top of the mp-TiO$_2$ layer and heated at 500 °C for 15 min.

2.2. SILAR growth of Ag$_8$SnS$_6$ nanocrystals

The formation of Ag–Sn–S nanocrystals was made by a two-stage SILAR process. In the first stage, Ag–S nanoparticles were grown on the mp-TiO$_2$ electrode. In the second stage, Sn–S nanoparticles were grown on top of the Ag–S nanoparticles. Post-annealing transformed the Ag–S/Sn–S double-layered structure into the Ag–Sn–S phase. An Ag–S SILAR cycle was performed by dipping the TiO$_2$ electrode in the solution of AgNO$_3$ (0.1 M) for 30 s accompanied with rinsing and drying the electrode. The step resulted in the adsorption of Ag ions on the pores of mp-TiO$_2$. The electrode was then dipped in a Na$_2$S (0.1 M) solution. This process is called one SILAR cycle and creates the Ag$_2$S nuclei. Repetition of this process is necessary to increase the particle size of Ag$_2$S nuclei. In the second-stage SILAR cycle for Sn–S, the same procedure was followed except changing the AgNO$_3$ cation precursor solution with SnCl$_2$ solution to make Sn–S. To achieve high performance, the numbers of Ag$_2$S and Sn–S SILAR cycles need to be optimized. The best ratio for Ag$_2$S and Sn–S SILAR cycles were found to be 3 : 2. For example, a sample with 12 Ag$_2$S cycles has 8 Sn–S cycles. To simplify discussion, a sample with Ag$_2$S (12 cycles)/Sn–S (8 cycles) will be referred to as sample with SILAR(12) herein. Finally, the Ag$_2$S/Sn–S deposited mp-TiO$_2$ electrode was annealed at 400 °C for 10 min under flowing N$_2$ gas, which resulted in the formation of ternary phase Ag$_8$SnS$_6$ nanoparticles.

2.3. Fabrication of solar cells

The solar cells were fabricated by a sandwich-type assembly of the Ag$_8$SnS$_6$ nanocrystal-immobilized TiO$_2$ photoelectrode and counter electrode (CE) using a 190 μm-thick parafilm thermoplastic spacer and sealant. Gold (Au) was used as the CE. A polysulfide electrolyte containing 0.5 M Na$_2$S, 2 M S, 0.2 M KCl and 0.5 M NaOH in a methanol/DI water (volume ratio 7 : 3) solution was used as a redox mediator. The cobalt electrolyte consisted of 0.2 M Co^{2+} (Co[PyPz]$_3$[PF$_6$]$_2$ salt-Dyesol), 0.05 M Co^{3+} (Co[PyPz]$_3$[PF$_6$]$_2$-Dyesol), 0.2 M LiClO$_4$, and 0.2 M t-butyl pyridine with acetonitrile solution, where Py is pyridine and Pz is pyrazole. The electrolyte was injected separately through a predrilled hole on the counter electrode into the cell. The Au CE film, ~70 nm in thickness, was deposited onto an FTO substrate by sputtering evaporation.

2.4. Material characterization and photovoltaic measurements

The crystal structure and phase purity of the prepared material were studied using a high-resolution X-ray diffractometer (XRD, Bruker D8 SSS). The particle size and morphology were determined by a transmission electron microscope (TEM, Joel JEM-2010). Optical properties were studied using a Hitachi U-2800A UV-Vis spectrophotometer. The photovoltaic performance was studied by measuring photocurrent–voltage (I–V) curves using a Keithley 2400 source meter under 100 mW cm^{-2} light illumination from an Oriel 150 W Xe lamp with an Oriel bandpass filter simulating the AM 1.5 solar spectrum. External quantum efficiency (EQE) was measured using the monochromatic light generated from an Acton monochromator with a 250 W tungsten halogen lamp. The active area, defined by a metal mask, was 3 mm × 3 mm.

3. Results and discussion

3.1. Morphology and crystal structure characterization

The structural property of the prepared Ag–Sn–S ternary phase was investigated by studying its X-ray diffraction (XRD) pattern after annealing at 400 °C under nitrogen atmosphere. The XRD pattern shown in Fig. 1 indicates the formation of orthorhombic Ag$_8$SnS$_6$ structure that is in agreement with the reference JCPDS no. 00-038-0434. The diffraction planes given at (311), (120), (411), (022), (122), (510), (313), (322), (123), (031), (611), (131), (603) and (424) are characteristic of the orthorhombic Ag$_8$SnS$_6$ structure. The (022) peak shows the strongest
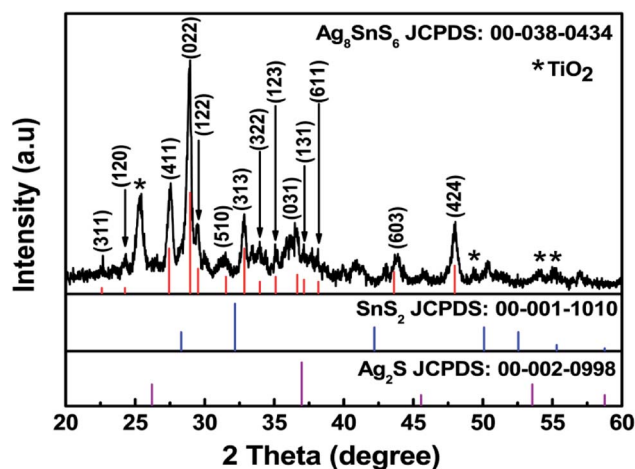

Fig. 1 XRD spectra of Ag$_8$SnS$_6$ nanocrystals along with the reference JCPDS 00-038-0434, reference patterns of SnS$_2$ and reference pattern of Ag$_2$S.

peak intensity compared with other peaks signifying the preferential orientation or major growth of the crystal along (022) plane. The other peaks due to the TiO_2 and FTO substrates were also observed. The calculated lattice constants for orthorhombic Ag_8SnS_6 are $a = 15.29$, $b = 7.57$ and $c = 10.71$ Å, which are in good agreement with the lattice constants of the data in the JCPDS database. For comparison, the major peaks associated with the binary Ag_2S and SnS_2 compounds are displayed in the bottom panel. It is clear the Ag_8SnS_6 XRD pattern does not contain the two starting binary phases, indicating successful formation of the Ag_8SnS_6 single phase. The deposited Ag–S/Sn–S double-layered particles are mostly amorphous before heat treatment (see Fig. S1, ESI†). Only a weak Ag_2S peak at 37° corresponding to the (200) plane can be observed. The average particle size of Ag_8SnS_6 nanocrystals, calculated by the Scherrer's formula[36] given in eqn (1) using the strongest (022) peak, is about 17.4 nm.

$$D = \frac{K\lambda}{\beta \cos \theta}, \tag{1}$$

where D is the average particle size, λ is the wavelength of the incident X-rays, β is the value of the full width at half maximum, K is a numerical constant and θ is the Bragg angle.

Fig. 2a displays a TEM image of bare TiO_2 nanoparticles. The rectangular shaped TiO_2 particles have round corners and an average length of 30 nm. Fig. 2b displays a TEM image of Ag_8SnS_6 nanocrystals grown on the surface of TiO_2 nanoparticles. The Ag_8SnS_6 nanocrystals, marked by red arrows, are randomly distributed all over the pores of mesoporous TiO_2 with no visible aggregation. Fig. 2c shows the size distribution of Ag_8SnS_6 nanocrystals prepared with eight SILAR cycles. The particle size of Ag_8SnS_6 nanocrystals is the range of ~10–20 nm with a distribution peak near 15 nm. This size is in agreement with the value (17 nm) calculated using Scherrer's formula.

3.2. Optical property

Fig. 3a shows the UV-Visible transmission spectra $T(\lambda)$ of Ag_8SnS_6 nanocrystals with different numbers of SILAR cycles n. The corresponding optical absorbance $A(\lambda)$, calculated from the optical transmission value using the relation $A(\lambda) = \log\left(\frac{1}{T}\right)$, is displayed in Fig. 3b. The transmission $T(\lambda)$ decreases with increasing n, indicating increasing light absorption by the increased amount of material with increasing SILAR cycles. The absorbance $A(\lambda)$ increases with increasing n, which is, again, the result of increasing material. A notable feature of the transmission spectra is that the small transmission ($T(\lambda) \leq 5\%$, $n = 12$ sample) for wavelengths < 700 nm. This implies the Ag_8SnS_6 nanocrystals can absorb nearly all the photon energy with wavelength lower than 700 nm (the visible and near IR regions of the solar spectrum). The large light absorption ability is an advantageous property for a solar material.

Fig. 3c shows the Tauc plot, $(\alpha h\nu)^2$ versus $h\nu$, of the Ag_8SnS_6 nanocrystals where h is the Planck constant and ν is the frequency. The optical band gap E_g can be estimated by finding the x-intercept of an extrapolated Tauc plot. E_g decreases with
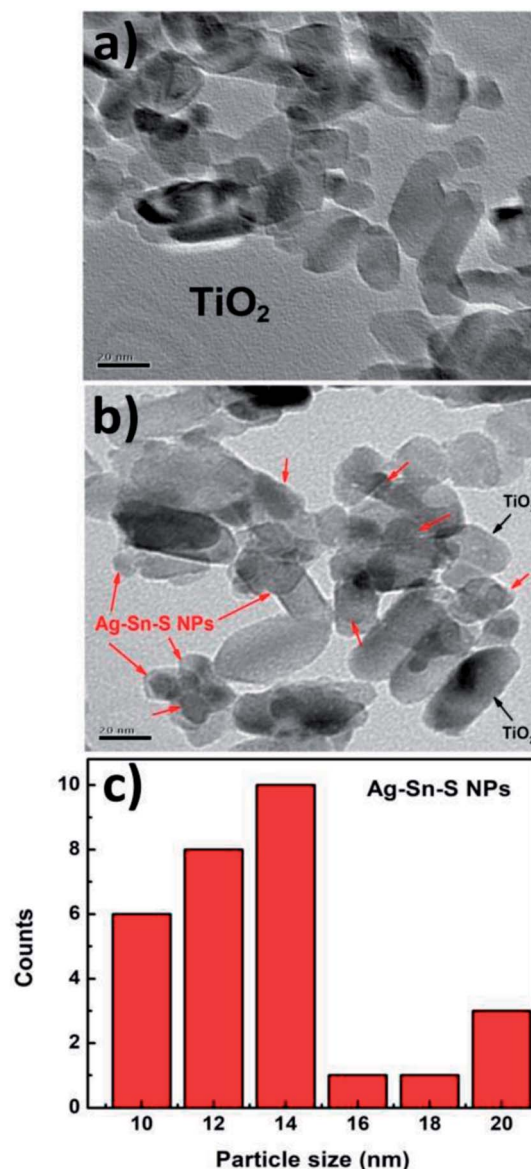

Fig. 2 TEM images of (a) 30 nm bare TiO_2 nanoparticles, (b) Ag_8SnS_6 nanocrystals deposited on TiO_2 nanoparticles and (c) size distribution of Ag_8SnS_6 nanocrystals.

increasing SILAR cycles n as: 1.76, 1.54, 1.41 eV for SILAR cycles of 6, 9, 12, respectively. The decrease in E_g with increasing n is attributed partly to the quantum size effect – a large SILAR cycle produced larger particles and, hence, a lower E_g. The E_g observed here is in agreement with the literature values for Ag_8SnS_6 nanocrystals prepared by other synthesis methods (1.31–1.45 eV).[31,33,35] Moreover, The E_g of 1.41 eV ($n = 12$ sample) is equal to the optimal E_g (1.4 eV) for a solar absorber, which is favorable property for a solar material.

3.3. Photovoltaic performance

The photovoltaic performance of a SILAR-prepared QDSSC is strongly dependent on the number of SILAR cycles n. An insufficient or excess amount of semiconductor absorber material leads to low efficiencies. Fig. 4 displays the J–V curves
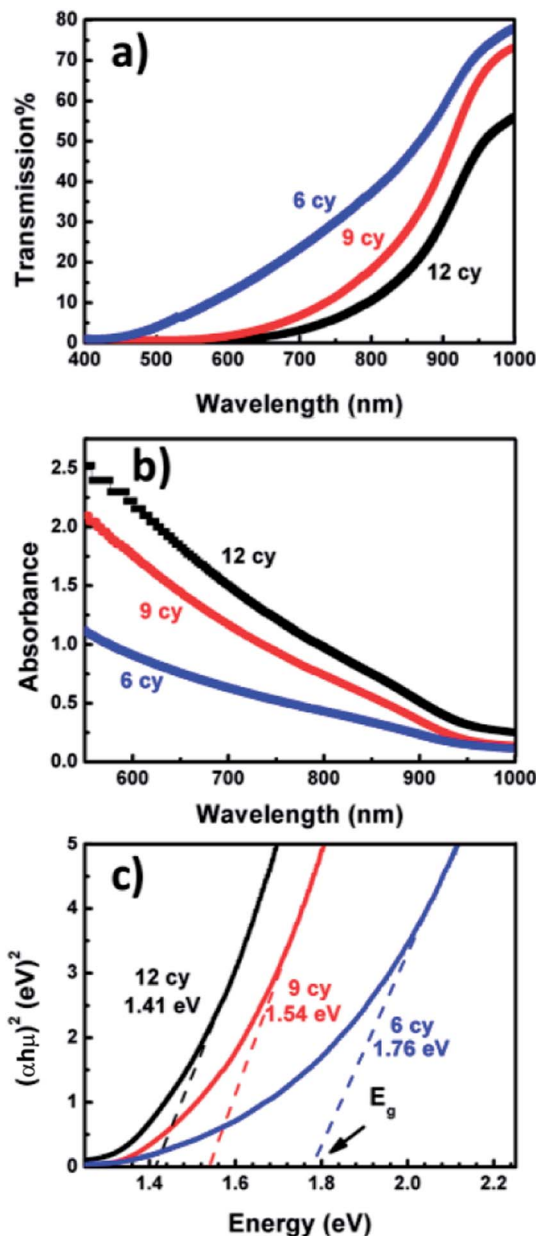
Fig. 3 Optical spectra (a) transmission, (b) absorbance and (c) Tauc plots $(\alpha h\nu)^2$ versus $h\nu$.

for Ag_8SnS_6 QDSSCs with various numbers of SILAR cycles n. The CE was Au and the electrolyte was polysulfide. Table 1 lists the photovoltaic parameters – short-circuit current density (J_{sc}), fill factor (FF), open-circuit voltage (V_{oc}) and power conversion efficiency (PCE). The efficiency increased with SILAR cycles n, reaching a maximal PCE of 0.68% at $n = 10$ (sample no. 3), then decreased again for a larger SILAR cycle of $n = 11$ (sample no. 4). The optimal sample (no. 3) has the photovoltaic parameters of $J_{sc} = 9.01$ mA cm^{-2}, open-circuit voltage $V_{oc} = 0.26$ V and FF = 28.9%. These are typical results for QDSSCs prepared by SILAR. Initially, the amount of material deposited on the mp-TiO_2 electrode was low, leading to insufficient solar light harvesting and low efficiencies. The deposited material increased with the SILAR cycle, leading to improved efficiencies. This result had
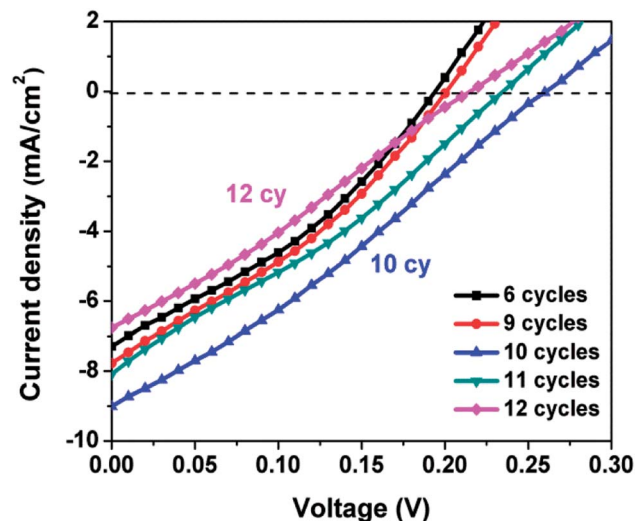

Fig. 4 J–V curves of Ag_8SnS_6 QDSSCs with various numbers of SILAR cycles n.

been observed in CdS and other semiconductor solar cells as reported previously.[37,38] After reaching the optimal SILAR cycle of 10, a further increase in SILAR cycle led to over-saturated material among the porous spaces within the mp-TiO_2 matrix, which hindered the flow of liquid electrolyte and led to a reduced efficiency.

The photovoltaic performance of a QDSSC could be improved by measuring J–V curves under reduced light intensities. Fig. 5 displays the J–V curves of the best Ag_8SnS_6 cell under various light intensities. The cell had an Au CE and a polysulfide electrolyte. Table 2 lists the photovoltaic parameters. As the incident light intensity was reduced from 100% sun to 10% sun, the PCE increased from 0.64% to 1.43%, a significant increase of 123%. The improved PCE is due to (a) an increase in FF from 31.3% to 39.7%, an improvement of 27%; and (b) an improvement in J_{sc} due to the reduction in carrier recombination (explained below). For an ideal solar cell, the current density J_{sc} should be linearly proportional to the number of incident photon n_{ph}. As the light intensity was reduced from 1 to 0.1 sun, the number of incident photons n_{ph} was also reduced to $0.1n_{ph}$. Hence, the linear response model predicted that J_{sc} at 0.1 sun should equal to 9.29 mA cm^{-2} (1 sun) × 0.1 = 0.929 mA cm^{-2}. However, the experimental data in Table 2 shows a much higher J_{sc} of 2.25 mA cm^{-2} under 0.1 sun. Semiconductor nanocrystals prepared by SILAR inherently contain a large number of surface defects, which act as

Table 1 Photovoltaic performance of Ag_8SnS_6 quantum dot-sensitized solar cells with various numbers of SILAR cycles. Electrolyte: polysulfide. Light intensity: 1 sun. Counter electrode: Au

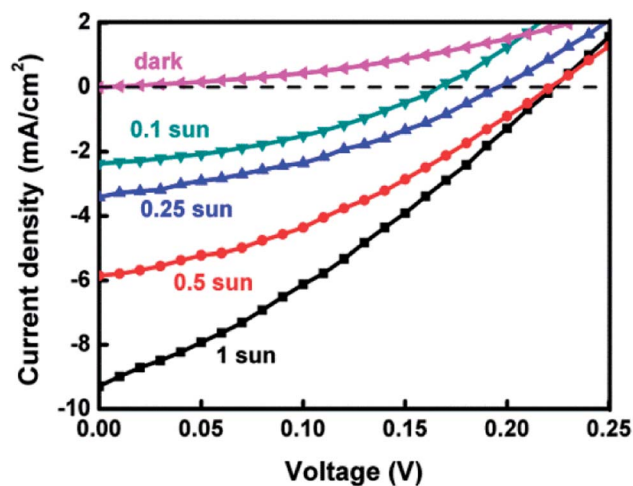| Sample no.	SILAR cycle	J_{sc} (mA cm^{-2})	V (V)	FF (%)	PCE (%)
1	6	7.29	0.19	34.07	0.47
2	9	7.77	0.20	32.45	0.50
3	10	9.01	0.26	28.90	0.68
4	11	8.08	0.23	30.25	0.56
5	12	7.62	0.24	29.91	0.55

Fig. 5 *J–V* curves of Ag$_8$SnS$_6$ QDSSCs under various light intensities. Electrolyte: polysulfide.

Table 2 Photovoltaic performance of Ag$_8$SnS$_6$ quantum dot-sensitized solar cells under various sun intensities

Sun intensity	J_{sc} (mA cm^{-2})	V_{oc} (V)	FF (%)	η (%)
100%	9.29	0.23	31.3	0.64
50%	5.85	0.22	35.4	0.92
25%	3.42	0.19	36.6	0.96
10%	2.25	0.16	39.7	1.43

recombination sites for photocarriers. The mechanism of recombination can be revealed by analyzing the dependence of J_{sc} on light intensity I_0. Analysis of the data in Table 2 yielded a sublinear relation: $J_{sc} \propto I_0^{\alpha}$ where $\alpha = 0.67$. Nelson has explained the sublinear J_{sc}–I_0 relation in terms of the multiple trapping model for carrier recombination.[39] A solar cell with multiple trapping would experience reduced carrier recombination at low light intensities and yield improved performance. The most important effect of low light intensities is the increase in electron lifetime τ_n under low light. Miyashita *et al.* and A. C. Fisher *et al.* had observed in dye-sensitized solar cells that τ_n increased by $\sim$3–10 times as the light intensity was decreased from 100 to 10% sun.[40,41] The significantly improved performance under low light intensities indicates that carrier recombination is the limiting process in the liquid-junction Ag$_8$SnS$_6$ sensitized solar cell at high incident light intensities. The competition between recombination and extraction of free charges determines FF, J_{sc} and inturn the PCE of the cell. At low light intensities, the charge carrier recombination process is reduced, which improves the charge extraction process and the performance of the solar cell.[42]

Reducing light intensities also has an effect on V_{oc}. As seen in Table 2, V_{oc} decreased monotonically with light intensity. As the light intensity decreased from 100% to 10% sun, V_{oc} decreased from 0.23 to 0.16 V. This can be explained as follows. The theoretical maximal V_{oc} of a QDSSC is the difference between the quasi Fermi level E_F of TiO$_2$ and the redox potential E_{redox} of the electrolyte, *i.e.*,

Table 3 Photovoltaic performance of Ag$_8$SnS$_6$ quantum dot-sensitized solar cells using a cobalt electrolyte

Light intensity	J_{sc} (mA cm^{-2})	V_{oc} (V)	FF (%)	PCE (%)
1 sun	3.20	0.54	30.61	0.528
0.1 sun	1.18	0.48	40.60	2.29

$$V_{oc} = E_F - E_{redox}. \tag{2}$$

The Fermi level E_F depends on the electron density n_{CB} in the conduction band (CB) of TiO$_2$ according to:[43]

$$E_F = k_B T \ln(n_{CB})$$

A reduced light intensity generates a reduced number of photoelectrons n_{CB}, leading to a lower E_F and V_{oc} as shown in Table 2.

A disadvantage of the Ag$_8$SnS$_6$ QDSSC is that the V_{oc} had a low value of 0.24 V, which lowered the attainable efficiency. One way to improve V_{oc} is to use a different electrolyte. As eqn (2) indicates, a lower redox potential E_{redox} will produce a higher V_{oc}. Here the polysulfide electrolyte in the Ag$_8$SnS$_6$ QDSSC was replaced by the cobalt electrolyte. Cobalt electrolytes have a redox level of 0.86 V relative to NHE (normal hydrogen electrode) whereas the polysulfide electrolyte has a redox level of -0.77 V.[44] The difference is 1.57 V. The cobalt electrolyte produced a much larger V_{oc} of 0.54 V (Table 3) under 1 sun, as compared to 0.24 V of the polysulfide electrolyte. The PCE of the cobalt-electrolyte Ag$_8$SnS$_6$ QDSSC is 0.53% under 1 sun. However, at the reduced light intensity of 0.1 sun, the PCE greatly increased to 2.29% (Fig. 6), which is 60% higher than that (1.43%) of the polysulfide cell.

A known disadvantage of cobalt electrolytes is its low diffusion coefficient and slow kinetics for hole transfer in electrolytes, resulting a low J_{sc}. So the cobalt electrolyte works better under low light intensities when the small number of photoelectrons is small. A cobalt electrolyte will produce a low J_{sc} and
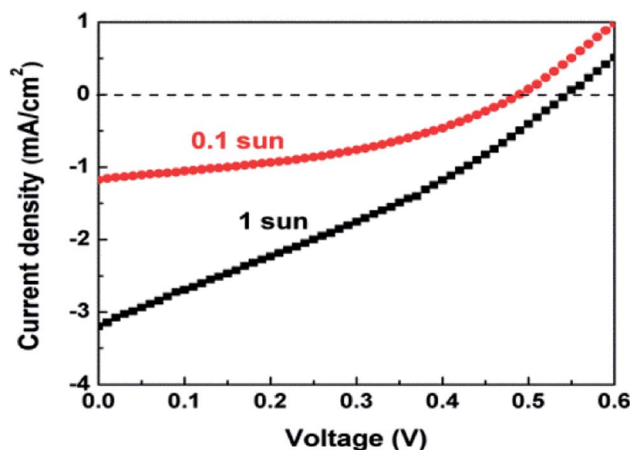

Fig. 6 *J–V* curves of an Ag$_8$SnS$_6$ QDSSC employing cobalt electrolyte under 1 and 0.1 sun.
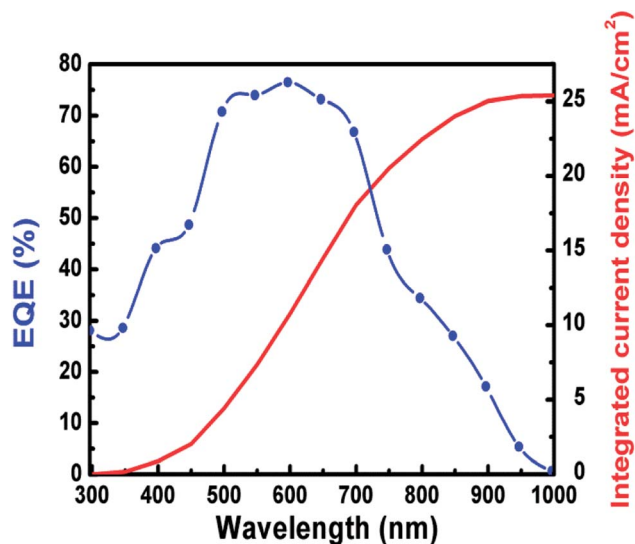
Fig. 7 EQE spectrum.

a high V_{oc}. The large gains in V_{oc} and FF compensate loss in J_{sc} and increase the PCE to 2.29% under 0.1 sun.

Fig. 7 displays the EQE spectrum for the best Ag_8SnS_6 QDSSCs in the 300–1000 nm wavelength range, where a maximum EQE value of 77% at $\lambda = 600$ nm was achieved. The cell started to produce a current at the onset wavelength of 1000 nm. The E_g of Ag_8SnS_6 nanocrystals, calculated from the onset wavelength of the EQE spectrum using the relation: E_g (eV) $= \dfrac{1240}{\lambda \ (nm)}$, is 1.24 eV, which is close to the optical E_g value of 1.41 eV shown in Fig. 4. Therefore, we conclude that the Ag_8SnS_6 nanocrystal has an E_g value of 1.24–1.41 eV. This E_g equals to the optimal E_g (1.4 eV) for a solar absorber, showing its potential as a solar absorber material. The area under the EQE curve represents the total integrated current density J_{ph} generated from the solar cell. J_{ph} can be calculated from the EQE curve using the following equation:

$$J_{ph} = e \int_{300}^{1000} \Phi(\lambda) \mathrm{EQE}(\lambda) \mathrm{d}\lambda,$$

where $\Phi(\lambda)$ is the incident photon flux and e is the elementary charge. The integrated EQE resulted in a maximum J_{ph} of 25.5 mA cm^{-2} (shown in the right axis of Fig. 7). The EQE measurement is basically equivalent to a low-light I–V measurement because the single-wavelength light dispersed from a monochromator has a relatively low power intensity. Compared to Table 2, the integrated J_{ph} of 25.5 mA cm^{-2} is consistent with the J_{sc} of 2.25 mA cm^{-2} under 0.1 sun (*i.e.* 25.5 × 0.1 sun = 2.55 mA cm^{-2}).

4. Conclusion

We demonstrated liquid-junction Ag_8SnS_6 QDSSCs prepared by SILAR on a mp-TiO$_2$ electrode. The orthorhombic Ag_8SnS_6 nanocrystals have an E_g of 1.24–1.41 eV and an average size of 15 nm. The cell employing polysulfide electrolyte exhibited a V_{oc} of 0.23 V, and a PCE of 1.43% at 0.1 sun. In contrast, the cell employing cobalt electrolyte yielded a higher PCE of 2.29% at 0. 1 sun. The near optimal E_g and the broad absorption band suggest that Ag_8SnS_6 nanocrystal could be a promising candidate material for solar cells.

Conflicts of interest

There are no conflicts to declare.

Acknowledgements

References

1 P. V. Kamat, *J. Phys. Chem. C*, 2008, **112**, 18737–18753.
2 A. Kongkanand, K. Tvrdy, K. Takechi, M. Kuno and P. V. Kamat, *J. Am. Chem. Soc.*, 2008, **130**, 4007–4015.
3 I. Moreels, K. Lambert, D. D. Muynck, F. Vanhaecke, D. Poelman, J. C. Martins, G. Allan and Z. Hens, *Chem. Mater.*, 2007, **19**, 3023–3030.
4 R. D. Schaller and V. I. Klimov, *Phys. Rev. Lett.*, 2004, **92**, 186601–186604.
5 R. J. Ellingson, M. C. Beard, J. C. Johnson, P. Yu, O. I. Micic, A. J. Nozik, A. Shabaev and A. L. Efros, *Nano Lett.*, 2005, **5**, 865–871.
6 V. I. Klimov, *J. Phys. Chem. B*, 2006, **110**, 16827–16845.
7 J. B. Sambur, T. Novet and B. A. Parkinson, *Science*, 2010, **330**, 63–66.
8 O. E. Semonin, J. M. Luther, S. Choi, H.-Y. Chen, J. Gao, A. J. Nozik and M. C. Beard, *Science*, 2011, **334**, 1530–1533.
9 W. A. Tisdale, K. J. Williams, B. A. Timp, D. J. Norris, E. S. Aydil and X.-Y. Zhu, *Science*, 2010, **328**, 1543–1547.
10 T. Zdanowicz, T. Rodziewicz and M. M. Zabkowska-Waclawek, *Sol. Energy Mater. Sol. Cells*, 2005, **87**, 757–769.
11 G. Larramona, C. Chone, A. Jacob, D. Sakakura, B. Delatouche, D. Pere, X. Cieren, M. Nagino and R. Bayon, *Chem. Mater.*, 2006, **18**, 1688–1696.
12 N. Guijarro, T. L. Villarreal, I. Mora-Seró, J. Bisquert and R. J Gómez, *J. Phys. Chem. C*, 2009, **113**, 4208–4214.
13 V. G. Pedro, C. Sima, G. Marzari, P. P. Boix, S. Giménez, Q. Shen, T. Dittrich and I. M. Seró, *Phys. Chem. Chem. Phys.*, 2013, **15**, 13835–13843.
14 Y. Itzhaik, O. Niitsoo, M. Page and G. Hodes, *J. Phys. Chem. C*, 2009, **113**, 4254–4256.
15 A. Tubtimtae, K. L. Wu, H. Y. Tung, M. W. Lee and G. J. Wang, *Electrochem. Commun.*, 2010, **12**, 1158–1160.
16 S. L. Castro, S. G. Bailey, R. P. Raffaelle, K. K. Banger and A. F. Hepp, *J. Phys. Chem. B*, 2004, **108**, 12429–12435.
17 T. Torimoto, T. Adachi, K. I. Okazaki, M. Sakuraoka, T. Shibayama, B. Ohtani, A. Kudo and S. Kuwabata, *J. Am. Chem. Soc.*, 2007, **129**, 12388–12389.
18 P. C. Huang, W. C. Yang and M. W. Lee, *J. Phys. Chem. C*, 2013, **117**, 18308–18314.

19 W. C. Yang and M. W. Lee, *J. Electrochem. Soc.*, 2014, **161**, H92–H96.

20 C. L. Chou, N. Suriyawonga, B. Aragawa, J. B Shib and M. W. Lee, *J. Electrochem. Soc.*, 2016, **163**, H445–H449.

21 Z. Jia, Q. Chen, J. Chen, T. Wang, Z. Li and X. Dou, *RSC Adv.*, 2015, **5**, 28885–28891.

22 H. D. Shelke, A. C. Lokhande, J. H. Kim and C. D. Lokhande, *J. Colloid Interface Sci.*, 2017, **506**, 144–153.

23 Q. Chen, X. Dou, Z. Li, Y. Ni, J. Chen, F. Zhou, Y. Yamaguchi and S. Zhuang, *Optik*, 2014, **125**, 3217–3220.

24 Y. Chen, L. Ma, Y. Yin, X. Qian, G. Zhou, X. Gu, W. Liu, X. Wu and F. Zhang, *J. Alloys Compd.*, 2016, **672**, 204–211.

25 C. L. Lu, Z. Lin, Y. W. Zhang, S. Y. Liu and M. Yang, *Chin. Phys. B*, 2015, **24**, 017501.

26 C. An, K. Tang, G. Shen, C. Wang, L. Huang and Y. Qian, *Mater. Res. Bull.*, 2003, **38**(5), 823–830.

27 B. Li, Y. Xie, J. Huang, H. Su and Y. Qian, *J. Solid State Chem.*, 2000, **149**(2), 338–340.

28 Q. Li, Y. Ding, X. Liu and Y. Qian, *Mater. Res. Bull.*, 2001, **36**, 2649–2656.

29 B. H. Shambharkar and A. P. Chowdhury, *RSC Adv.*, 2016, **6**, 10513–10519.

30 M. Deng, S. Shen, Y. Zhang, H. Xu and Q. Wang, *New J. Chem.*, 2014, **38**, 77–83.

31 Q. He, S. Huang, C. Wang, Q. Qiao, N. Liang, M. Xu, W. Chen, J. Zai and X. Qian, *ChemSusChem*, 2015, **8**, 817–820.

32 W. Q. Hu, Y. F. Shi and L. M. Wu, *Cryst. Growth Des.*, 2012, **12**, 3458–3464.

33 K. W. Cheng, W. T. Tsai and Y. H. Wu, *J. Power Sources*, 2016, **317**, 81–88.

34 T. Ghrib, A. L. A. Otaibi, M. A. Almessiere, I. B. Assaker and R. Chtourou, *Chin. Phys. Lett.*, 2015, **32**, 127402.

35 L. Zhu, Y. Xu, H. Zheng, G. Liu, X. Xu, X. Pan and S. Dai, *Sci. China Mater.*, 2018, **61**, 1549–1556.

36 A. L. Patterson, *Phys. Rev.*, 1939, **56**, 978–982.

37 M. Ganjian, M. Kolahdouz, A. Aletayeb, M. Norouzi, P. Ebrahimi, S. Pourjafari and M. S. S. Mousavi, *Vacuum*, 2017, **146**, 548–553.

38 M. Marandi, E. Rahmani and F. A. Farahani, *J. Electron. Mater.*, 2017, **46**, 6769–6783.

39 J. Nelson, S. A. Haque, D. R. Klug and J. R. Durrant, *Phys. Rev. B: Condens. Matter Mater. Phys.*, 2001, **63**, 205321–205329.

40 M. Miyashita, K. Sunahara, T. Nishikawa, Y. Uemura, N. Koumura, K. Hara, A. Mori, T. Abe, E. Suzuki and S. Mori, *J. Am. Chem. Soc.*, 2008, **130**, 17874–17881.

41 A. C. Fisher, L. M. Peter, E. A. Ponomarev, A. B. Walker and K. G. U. Wijayantha, *J. Phys. Chem. B*, 2000, **104**, 949–958.

42 D. Bartesaghi, I. C. Pérez, J. Kniepert, S. Roland, M. Turbiez, D. Neher and L. J. A. Koster, *Nat. Commun.*, 2015, **6**, 7083.

43 J. Nelson, *The Physics of Solar Cells*, Imperial College Press, London, 2003, p. 59, DOI: 10.1142/p276.

44 F. Hao, P. Dong, Q. Luo, J. Li, J. Lou and H. Lin, *Energy Environ. Sci.*, 2013, **6**, 2003–2019.